Progress Report on the Proposal

to Build an Off-Axis Detector

to Study $\nu_\mu \rightarrow \nu_e$ Oscillations

in the NuMI Beamline

(P929)

December 2, 2003

The NuMI Off-Axis Collaboration

Argonne, Athens, Caltech, UCLA, Cambridge, Fermilab,
College de France, Harvard, Indiana, ITEP, Lebedev,
Louisiana State, MIT, Michigan State, Minnesota/Duluth,
Minnesota/Minneapolis, Munich, Stony Brook,
Northern Illinois, Ohio, Oxford, Rio de Janeiro, Rochester,
Rutherford, South Carolina, Stanford, Texas A&M,
Texas/Austin, Tufts, Virginia Tech, William & Mary,
Wisconsin, York

I. Ambats, D. S. Ayres, J. W. Dawson, G. Drake, M. C. Goodman, J. J. Grudzinski,
V. J. Guarino, T. Joffe-Minor, D. E. Reyna, R. L. Talaga, J. L. Thron, R. G. Wagner
Argonne National Laboratory, Argonne, IL

D. Drakoulakos, N. Giokaris, P. Stamoulis, S. Stiliaris, G. Tzanakos, M. Zois
University of Athens, Athens, Greece

B. Barish, J. Hanson, D. G. Michael, H. B. Newman, C. W. Peck, C. Smith, J. Trevor,
H. Zheng
California Institute of Technology, Pasadena, CA

D. B. Cline, H. Wang, Y. Chen, K. Lee, Y. Seo, X. Yang
University of California, Los Angeles, CA

M. Thomson
University of Cambridge, Cambridge, United Kingdom

R. Bernstein, G. Bock, L. Camilleri*, S. Childress, B. Choudhary, J. Cooper, R. Hatcher,
D. Harris, J. Hylen, H. Jostlein, J. Kilmer, P. Lucas, A. Marchionni, O. Mena, A. Para,
S. Parke, S. Pordes, R. Rameika, R. Ray, R. Schmitt, P. Shanahan, P. Spentzouris,
R. Wands
Fermi National Accelerator Laboratory, Batavia, IL

T. Patzak, R. Piteira
College de France, Paris, France

G. J. Feldman**, N. Felt, A. Lebedev, J. Oliver, M. Sanchez, S.-M. Seun
Harvard University, Cambridge, MA

C. Bower, M. Gebhard, M. D. Messier, S. Mufson, J. Musser, B. J. Rebel, J. Urheim
Indiana University, Bloomington, IN

I. Trostin
Institute For Theoretical And Experimental Physics, Moscow, Russia

V. Ryabov, A. Y. Terekhov
P. N. Lebedev Physical Institute, Moscow, Russia

W. Metcalf
Louisiana State University, Raton Rouge, LA

K. Scholberg
Massachusetts Institute of Technology, Cambridge, MA

C. Bromberg, J. Huston, R. Miller, R. Richards
Michigan State University, East Lansing, MI

A. Habig
University of Minnesota, Duluth, MN

T. Chase, K. Heller, P. Litchfield, M. Marshak, W. Miller, L. Mualem, E. Peterson,
D. Petyt, K. Ruddick, R. Rusack
University of Minnesota, Minneapolis, MN

P. Huber, M. Lindner, W. Winter
Technische Universität München, Munich, Germany

R. Shrock
State University of New York, Stony Brook, NY

C. Albright
Northern Illinois University, DeKalb, IL

C. R. Brune, D. S. Carman, K. H. Hicks, S. M. Grimes, A. K. Opper
Ohio University, Athens, OH

G. Barr, J. H. Cobb, K. Grzelak, N. Tagg
University of Oxford, Oxford, United Kingdom

H. Nunokawa
Pontifícia Universidade Católica do Rio de Janeiro, Rio de Janeiro, Brazil

A. Bodek, H. Budd, S. Manly, K. McFarland, W. Sakumoto
University of Rochester, Rochester, NY

T. Durkin, R. Halsall, T. Nicholls, G. F. Pearce, A. Weber
Rutherford Appleton Laboratory, Chilton, Didcot, United Kingdom

T. Bergfeld, K. Bhaskaran, A. Godley, S. R. Mishra, C. Rosenfeld, K. Wu
University of South Carolina, Columbia, SC

S. Avvakumov, G. Irwin, S. Murgia, S. Wojcicki, T. Yang
Stanford University, Stanford, CA

E. Tetteh-Lartey, M. Watabe, R. Webb
Texas A&M University, College Station, TX

J. Klein, S. Kopp, K. Lang, M. Proga
University of Texas, Austin, TX

H.R. Gallagher, T. Kafka, W.A. Mann, J. Schneps
Tufts University, Medford, MA

F. F. Chen, K. Creehan, N. K. Morgan, L. Piilonen, R. H. Sturges, R. B. Vogelaar
Virginia Polytechnic Institute and State University, Blacksburg, VA

J. K. Nelson
The College of William and Mary, Williamsburg, VA

A.R. Erwin, C. Velissaris
University of Wisconsin, Madison, WI

S. Menary
York University, Toronto, Ontario, Canada

* On leave from CERN
** Contact person (chair of the Technical Steering Committee)

Introduction

A little over a year ago, we submitted a letter of intent to propose an off-axis experiment in the NuMI beam line, (P929). In the intervening time, we have been working towards a formal proposal. Our main activities have been
(1) the development of two detector concepts based on different technologies and two variants for each technology,
(2) simulations of these detectors,
(3) a detailed costing exercise for each of the technologies and variants,
(4) the selection of a baseline technology based on performance and cost,
(5) a (paper) study of backgrounds in a surface detector,
(6) consideration of the best strategy for a near detector,
(7) exploration of possible sites, and
(8) a study of the physics reach of the experiment.

We have also written a draft of a proposal. However, at this point, the draft is not as complete as we (and you) would like it to be. In particular, there are aspects of the costing and simulation work that we would like to improve. Thus, in consultation with the Laboratory management, we have decided to submit this progress report to you now with the full proposal to be submitted in advance of your April meeting.

Overview

The primary goal of the off-axis experiment will be to measure $\nu_\mu \rightarrow \nu_e$ oscillations at the atmospheric oscillation length with a three standard deviation discovery threshold an order of magnitude more sensitive than can be achieved with the MINOS experiment. The detection of this signal is necessary for the exploration of the three parameters of neutrino mixing about which we have no information: $\sin^2(2\theta_{13})$, the mass ordering of the mass doublet and mass singlet that participate in the atmospheric oscillations, and the CP-violating phase δ.

In order to meet this goal we are proposing three improvements over MINOS:

(1) A 50 kT far detector, approximately 10 times the MINOS mass. The challenge here is to reduce the cost per kT as much as possible, which we believe could be as much as a factor of three.
(2) A detector better optimized for the detection and identification of electrons. A medium-Z sandwich detector provides good separation of neutral current and electron charged-current events, as will be discussed below.
(3) Siting the experiment off the axis of the NuMI beam, resulting in a narrow-band neutrino beam. The advantages of such a beam are that the neutrino flux near the energy of the oscillation maximum is greater than can be achieved in an on-axis beam and that backgrounds from high-energy neutral current events are significantly reduced.

Technology Decision

A great deal of work during the past year has been devoted to developing and evaluating detailed designs using different detector technologies.   We did not consider non-sampling devices such as liquid argon TPC or water Cerenkov detectors. Although liquid argon shows great promise for neutrino detection, we felt that the required R&D efforts would not be compatible with the time scale on which we would like to construct this detector. Our simulations showed that, at our energies, water Cerenkov detectors are not sufficiently effective in separating electrons from leading neutral pions from neutral current events.

We were thus lead to tracking calorimeters made from sandwiches of medium-Z absorber and active detectors. With about 1/3 radiation length longitudinal granularity and 4 cm transverse segmentation, an electron appears as a "fuzzy" track in such a detector, with approximately 1.6 strips per plane hit. A muon or non-interacting pion appears as a sharper track with close to one strip per plane hit. The major problem in event identification, however, is the separation of electron charged current events from neutral current events in which the hadronic energy is dominated by a single neutral pion. The neutral current event has two photon conversions resulting in wider and less longitudinally concentrated electromagnetic showers and in gaps between the event vertex and the two conversion points. We will discuss the results of event simulations below.

The two technologies we developed were scintillator strips and glass resistive plate chambers (RPCs). The former was studied in two variants, one using solid scintillator and the other using liquid scintillator. In both forms, signals are read out from the scintillators by U-shaped wavelength-shifting fibers (WSFs) in to a multi-pixel avalanche photodiode (APD).   The solid scintillator modules are very similar to the MINOS modules. The liquid scintillator modules are made from 30-cell polyvinyl chloride (PVC) extrusions, loaded with 10-15% titanium dioxide for reflectivity.

The RPC design closely resembles the chambers used very successfully by the BELLE collaboration. The chambers are double layered with dimensions 2.84 x 2.42 m. The RPCs offer the possibility of two spatial dimensions of readout for every detector plane location.

To decide on a baseline technology, we considered three factors: technical risk, performance, and cost. Our object was to choose the technology with the lowest cost for a fixed performance, provided it had acceptably low technical risk. Both scintillator and RPC detectors appear to have acceptable levels of risk. The RPCs have been used successfully by the BELLE experiment and the performance of solid scintillator strips with WSF readout is well understood from the MINOS experiment. The new element in the scintillator detector is the APD readout, which combines the advantages over photomultipliers of lower cost and much higher quantum efficiency. However, we are able to piggyback off the work of the CMS collaboration, which is using similar APDs to

readout its electromagnetic calorimeter. Nonetheless, the liquid scintillator option with APD readout is the least tested of the possible options and needs to be subjected to a full-scale test to verify it performance. We hope to complete such a test in the next year.

We evaluated performance with full simulations starting with calibrated data from the detectors through the whole analysis chain.   Likelihood functions were constructed for signal events and an optimum cut on the likelihood was used to separate electron charged current events from all backgrounds. The optimum cut was set by maximizing a figure of merit (FOM) defined to be the signal divided by the square root of the background.

Differences in performance between the scintillator and RPC detectors come primarily from two sources: The RPC detectors have the advantage that both x and y readouts are potentially available at each chamber location, while the scintillator strips have inherently one dimensional readout in each plane.   The most recent simulation indicates that the gain in the FOM from two-dimensional readout is 13±3%. Since an earlier simulation indicated a smaller gain (3±7%), we have costed the RPC option with both one and two-dimensional readouts. The second difference between the two detectors is that the scintillators provide pulse height information on each strip while the RPCs provide only binary information since the signals are saturated.   The APDs' high quantum efficiency results in a sizeable number of photoelectrons per minimum ionizing particle. In the worst case, an interaction at the far end of a strip, we predict that in the current design we will obtain 28 photoelectrons. The gain in reading out an analog rather than binary signals has been calculated to be 5.4±2.4% in the FOM. Thus, the differences in performance of the two detectors are small, with a possible advantage to the RPC detector with two-dimensional readout. Additional simulations should provide increased resolution on performance gains.

An important consideration in our technology choice is the relative cost of the various detector options. We have done a detailed costing exercise, which is nonetheless still preliminary. Raw materials, for the most part, have been estimated from recent procurement experience or vendors' quotes. Required labor has, when possible, been estimated from previous experience. Estimates for the buildings and outfitting are very preliminary.

Table 1 lists our current working estimates of the various options. We have used percentages to include the multipliers of EDIA, project management overhead and contingency. This is at best a zeroth-order approximation. We are working on assigning these multipliers on an item-by-item basis.

At this time the liquid scintillator detector appears to be less expensive that the second cheapest option, RPCs with one-dimensional readout at each chamber location. The main difference comes from the amount of labor needed to assemble the modules. This is due to the fewer number of steps in the liquid scintillator module assembly. However, whereas there is experience in building solid scintillator modules from MINOS and from building glass RPCs from BELLE, there is not equivalent experience in building liquid scintillator modules from PVC extrusions. Thus, we need to verify the

time and effort estimates for liquid scintillator fabrication during the next year.   We also need to spend considerably more effort in evaluating the costs associated with the delivery, mixing and distribution of the liquid scintillator at the detector site.

Item	RPC 2-D readout	RPC 1-D readout	Solid scintillator	Liquid scintillator
Absorber	12.6	12.6	13.3	12.1
Active Detector M&S	40.7	36.2	57.9	29.2
Active Detector labor	16.3	14.5	20.3	7.3
Readout and DAQ	8.3	4.5	6.1	5.0
Shipping	2.2	2.2	3.0	1.0
Installation	2.6	2.6	5.8	4.7
Enclosure	25.0	25.0	28.0	31.0
Sub-total	107.7	97.6	134.4	90.3
EDIA (25%)	26.9	24.4	33.6	22.6
Project management (8%)	8.6	7.8	10.8	7.2
Overhead (20%)	21.5	19.5	26.9	18.1
Contingency (40%)	43.1	39.0	53.8	36.1
Total	207.9	188.4	259.4	174.3

Table 1. Estimated costs for four detector options in FY04 M$. The cost of a near detector is not included.

Since the liquid scintillator option appears to have a cost advantage over all other options and a small performance advantage over the next least expensive option, RPCs with one-dimensional readout per chamber location, it was our choice for the baseline technology. However, the R&D efforts projected for next year should provide significant new technical information, improved and more readily comparable results from simulations, and more reliable cost estimates. It is our intention to revisit the technology choice at that time to see if the selection of liquid scintillator is the still the optimum way to proceed.

Liquid Scintillator Detector

We will briefly describe the baseline liquid scintillator design here and give a brief description of the other options in the appendices. The liquid scintillator design has three distinct and mostly independent systems— the absorber structure, the active detector modules and the photodetector with electronics.

Absorber Structure

The proposed absorber is wood in the form of sheets of a manufactured wood product, either particleboard or oriented strand board (OSB), whichever is least expensive. For our purposes, these two products are equivalent and which one we would actually use will depend on availability and delivered price. In this report, we will use

these terms interchangeably. In addition to its properties of low density and medium Z, particleboard has sufficient structural strength to provide much of the required detector support structure. High efficiency, industrial strength fastening systems, such as quick-set, high-strength adhesives and cartridge-loaded screw guns, exist to install the fasteners required to assemble a particleboard structure. The overall detector design thus incorporates the active scintillator modules into what is functionally a large monolithic block of wood.

To take advantage of standard particleboard tooling, the detector will be sized in feet. The detector cross-section will be 48 feet high by 96 feet wide. Scintillator modules, 48 feet in length, will be embedded into the particleboard structure and arranged to give alternate orthogonal views separated by about 1/3 of a radiation length of absorber. This detector design and aspect ratio optimizes the detector with respect to cost and ease of construction.

The detector consists of 750 planes. Each plane consists of 12 stacks. Each stack is 48 feet (14.63 m) long by 8 feet (2.44 m) wide. Each stack consists of a laminate of 7 layers of particleboard and one layer of 2 PVC extrusions containing liquid scintillator. The layers of both particleboard and extrusions are 1.125 inches (2.86 cm) thick. Alternate layers are arranged with the extrusions in the horizontal and vertical directions, as illustrated in Fig. 1.

The active and passive layers are offset in order to create a rigid structure, as shown in Fig. 2. Also shown are edge brackets, which position and hold the active detector modules and provide structural stability to the stack, so that it can be lifted. Adjacent units and successive planes are screwed to each other for lateral stability while the load of the structure is transferred to the floor through the particleboard itself. A preliminary ANSYS finite element analysis shows that the structure will have sufficient integrity.

We expect to fabricate the passive absorber modules at the laboratory site. This assembly plan for detector construction is modeled on the successful MINOS experience. The lighter active elements will be manufactured away from the detector laboratory and shipped to the site. The active elements and the particleboard will be combined on-site as the detector is assembled.

Active Detector Elements

The geometry of the active detector elements is similar to that used in MINOS, but for the off-axis detector, the scintillator cells will be nearly twice as long and are read out only at one end. The scintillator is contained in titanium dioxide loaded PVC extrusions, each 48 feet (14.63 m) in length, 4 feet (1.22 m) in width and 1.125 in (2.86 cm) thick. Each extrusion contains 30 channels, with 1 mm internal walls and 1.5 mm external walls. PVC extrusions with 10 to 15% TiO_2 loading have been measured to have 96.5% reflectivity at 425 nm.
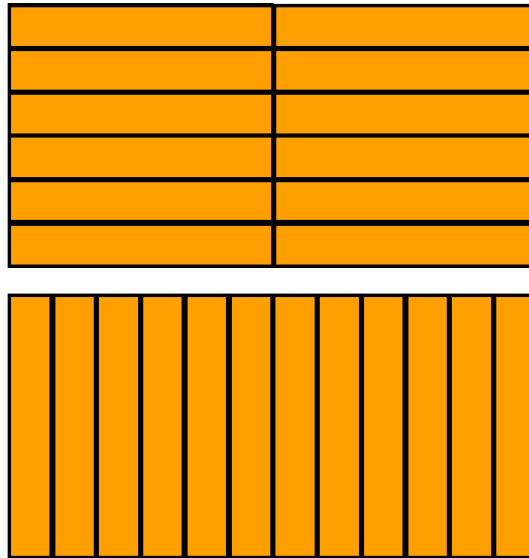
Figure 1. Layout of stacks showing arrangement of alternating layers. Each stack contains two scintillator modules.
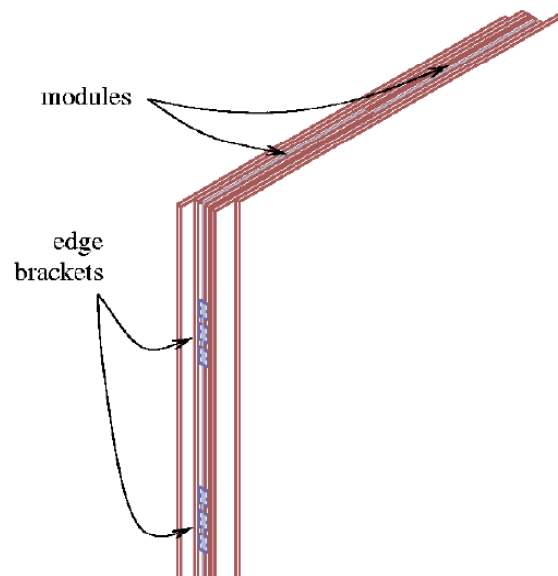

Figure 2. Stack design showing placement of the active modules and the offset structure.

Like the MINOS detector, the active detector modules will use wavelength-shifting fibers (WSFs) to transmit the light produced in a long cell of scintillator. Experience with the MINOS far detector provides extensive data on the performance of plastic scintillator with cells of cross-section 3.75 cm x 1 cm. Thicker cells (~4 cm x ~3 cm) will reliably give at least the same performance for liquid scintillator at substantially lower cost. The light transmitted down the fiber from the far end will be increased in comparison with MINOS by having a single fiber make two passes through the scintillator with a loop at the bottom. This configuration enables single-ended fiber readout, reducing the number of readout channels, and yielding four times as much light as would be observed from the far end of single fiber without a reflector.

There are three operations involved in making modules from the delivered extrusions: fiber insertion, end-cap attachment, and manifold attachment.

(1) Fiber insertion. One looped fiber will be inserted into each of the 30 cells in a single extrusion with a machine designed for the purpose.

(2) End-cap attachment. The non-readout end of the extrusion must be sealed to contain the liquid scintillator. Two possible arrangements will be tested. In one design, the extruder will simply pinch off one end of each extrusion as part of the process of cutting the extrusion to length. A second design is to seal the non-readout end of each extrusion by gluing on an endcap that permits liquid scintillator to flow from one cell to another, to promote rapid filling.

(3) Manifold attachment. The fiber manifold is likely the most complex mechanical element of the liquid scintillator detector design. It has several purposes. It guides the wavelength-shifting fibers from each cell to the readout connector. It light seals the end of the module. It facilitates filling of the module. It provides a buffer volume for the thermal expansion of the liquid scintillator. Figure 3 shows the design for a prototype manifold to guide the fibers from the end of a module to a bulk optical connector.

Photodetectors

The proposed photodetectors are avalanche photo-diodes (APDs) of a similar type to those used in the CMS Detector at the LHC. They are commercially available in large quantities from Hamamatsu. One APD pixel will be used for each scintillator cell. APDs have almost an order of magnitude higher quantum efficiency than the photocathode in photomultiplier tubes (PMTs) for the wavelengths that are less attenuated by a long wavelength shifting fiber, as shown in Fig. 4. APDs are also significantly less expensive than PMTs. The cost per channel in bare die form in the quantities appropriate for this experiment is $2.70 per channel, to be compared with a cost of about $12 for similar quantities of multi-channel PMTs. Figure 5 shows a photograph of the 32 pixel Hamamatsu APD array.

We expect to operate the APDs at a gain of 100. This low gain requires a high gain electronic amplifier, integrated with the necessary shaping, timing, gating, and pulse height measuring circuitry. Such amplifiers have been developed and produced in quantity for silicon strip detectors. The architecture we are considering is based on the Fermilab MASDA chip and the SVX4. In this design, the signal will be amplified by a
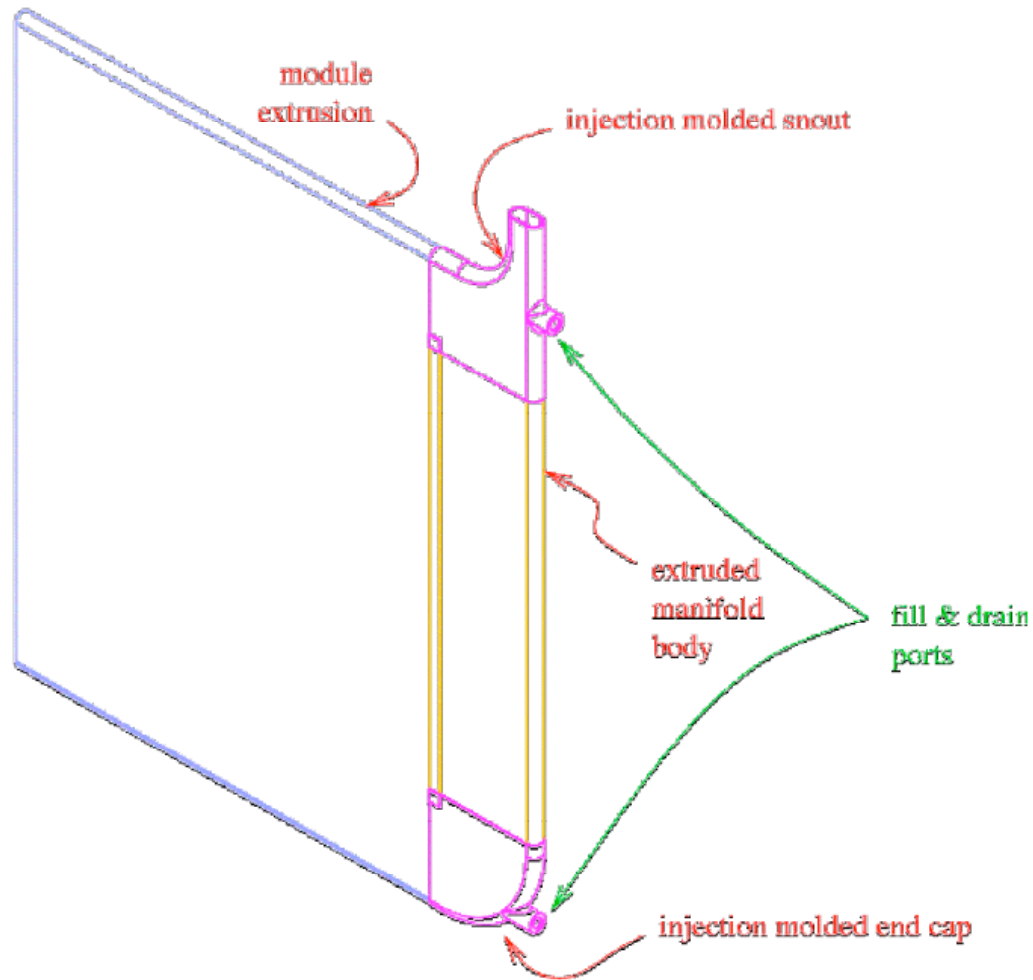
Figure 3. Prototype manifold to lead fibers from the ends of
scintillator cells to an optical connector.

high gain integrating amplifier with an RC time constant of ~350 ns. The amplifier output
will be gated into a switched capacitor array every 500 ns. At the end of beam spill, the
signals in each capacitor will be routed via an analog multiplexer to a 40 MHz 10-bit
ADC, with one ADC for each 32 APD channels. Trigger primitives will be constructed
locally and sent to a trigger processor. In the event of an interesting event, all of the event
data will be read out.

    To reduce the thermal noise of the APDs, it will be necessary to cool them to
approximately 0° F using an electronic Peltier circuit mounted on each APD array.
Calculations based on the measured performance of individual elements of the APD,
electronics, and cooling systems show that a signal to noise ratio of about 5:1 is
achievable for minimum ionizing particles at the far end of a scintillator strip.
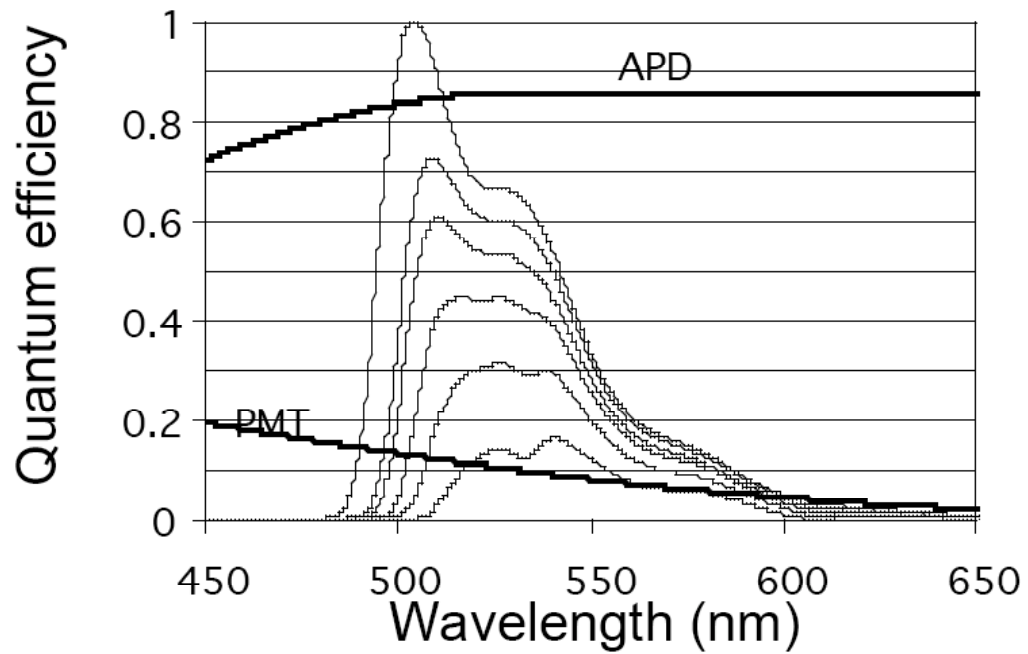
Figure 4. Quantum efficiencies of APD and PMT (bialkali photocathode) as a function of wavelength. Also shown are WLS fiber emission spectra measured at lengths of 0.5, 1, 2,4, 8, 16 m, illustrating the shift of the average emission wavelength as attenuation (fiber length) increases.
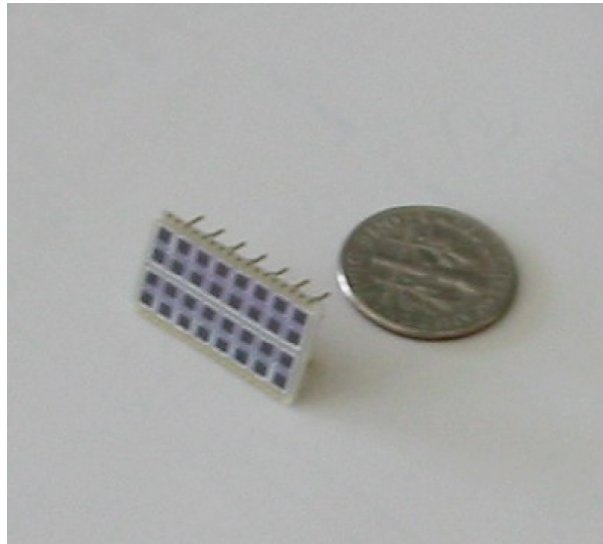

Figure 5. Hamamatsu 32-channel APD array, shown with a dime.

Table 2 summarizes the parameters of the baseline detector.

Detector mass	50 kT
Active detector mass	8.3 kT
Detector height	14.63 m
Detector width	29.26 m
Detector length	172 m
Absorber	Particleboard or OSB
Absorber density	0.70 g/cc
Active detector	Liquid scintillator Bicron BC517L
Active detector module (ADM)	30-cell PVC extrusion
Active detector module length	14.63 m
Active detector module width	1.22 m $\Rightarrow$ cell width = 4.07 cm
Active detector module thickness	2.86 cm
Number of planes	750
Number of stacks per plane	12
Number of ADM per stack	2
Total number of ADMs	18,000
Total number of cells	540,000

Table 2. Parameters of the baseline detector.

Enclosure

The far detector requires a building ~200 m long by ~40 m wide by ~20 m high. We anticipate constructing a 20-year life, metal-sided and roofed building, similar to the usual experimental area buildings located at accelerator laboratories. The building will be insulated, heated to ~60° F in the winter and cooled to ~80° F in the summer. Some humidity control is required to minimize expansion and contraction of the particleboard in the detector. A small control room and work area will be climate-controlled to usual office or laboratory standards. At the present time, we do not anticipate using earth shielding around or over the detector building. Sufficient earth shielding to have a significant effect would increase the cost of the building significantly. However, we need to verify experimentally that we can run the proposed detector without earth shielding, as will be discussed below.

Far Detector Site

We have examined more than a dozen possible sites for the far detector as well as multiple detector locations within several particular sites. Possible sites begin about 710 km from Fermilab, near the city of Aurora, MN, and continue to the north-northwest until a point in Ontario that is about 900 km from Fermilab. More distant sites are too far off-axis to have desirable beam characteristics because of the beam's upward inclination of ~3° and the curvature of the earth.

The principal site selection criteria are

(1) The site should be approximately 13±2 km off-axis from the NUMI beam. The optimum transverse position depends on Δm_{23}^2, but it is not critically dependent on it. For example, a site optimized for $\Delta m_{23}^2 = 2.5\times10^{-3}$ eV^2 will have a figure of merit (FOM) that is only 2.4% off maximum if Δm_{23}^2 turns out to be 2.0×10^{-3} eV^2. For fixed Δm_{23}^2 the optimum transverse position is also fairly broad. There is at least a 3 km interval in which the FOM does not vary from the maximum by more than 2%.

(2) The site should be as far as practical from Fermilab. Without the matter effect, the optimum FOM would be relatively independent of the distance. The flux falls off as $1/L^2$, giving a $1/L$ dependence to the FOM, which is canceled by the linear rise of the cross section with energy. However, the maximum length beam has the largest matter effect, which is necessary for the determination of the mass hierarchy.   It also enhances the neutrino oscillation for the normal mass hierarchy.

(3) The site should have year-round road access at the maximum trunk highway weight limit, adequate electrical power and T-3 capable communications access. Other geographic criteria include access to workers, road transportation and airports and proximity to support services such as hotels, restaurants, gasoline and other retail outlets.

(4) The site should have at least 20 acres of usable land and permit a layout of a ~200 m by ~40 m footprint for a detector building oriented with its long axis pointing towards Fermilab.

(5) The site should enjoy strong local support and its selection should be unlikely to result in land use controversies or litigation. The characteristics of the site should also facilitate a straightforward environmental permitting process. Although the University of Minnesota has authority to determine zoning and permitting with respect to its property within Minnesota, minimal land use controversy will facilitate the laboratory construction.

The three most suitable sites are, from south to north,

(1) on the Orr-Buyck Road (St. Louis County Highway 23) near the west end of Kjostad Lake, 775 km from Fermilab,

(2) on the Ash River Trail (St. Louis County Highway 129) near the entrance to Voyageur's National Park, 810 km from Fermilab and,

(3) on Ontario Highway 11 north of Rainy Lake near Mine Centre ON (about 60 km east of Fort Frances ON), 850 km from Fermilab.

The location of these sites is shown in Fig. 6. All three appear to meet the criteria listed above. The Ash River Trail site is the furthest site in the United States and is our baseline site. We have identified six suitable locations for the detector building on this site, ranging from 12.0 to 14.5 km off-axis. Two of the locations are on land owned by the Boise Cascade Corporation; the remaining four locations are on land owned by the State of Minnesota. At this time, the University of Minnesota is taking preliminary steps towards land acquisition and environmental review of these sites. Our current strategy is to defer a specific selection among the six locations at the Ash River site, as well as the choice of that site, for as long as possible, in order to have the best possible understanding of the relevant neutrino oscillation parameters before making a specific site selection.
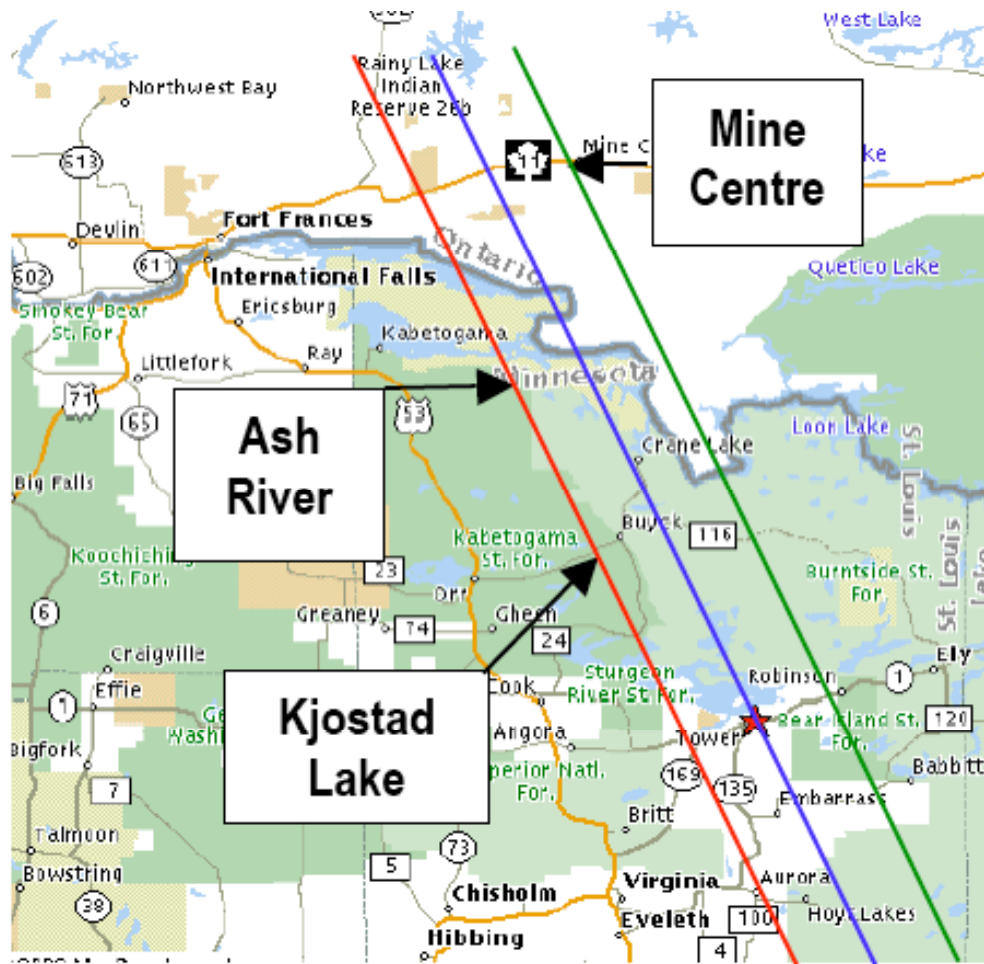
Figure 6. Map showing the location of the three preferred sites. The star indicates the site of the Soudan Underground Laboratory. The beam centerline passes through Soudan; the left line is 13 km west of the centerline, while the right line is 13 km east of the centerline.

The Mine Centre site is the only practical site in Canada. It is located on Crown (public) land. This site offers the possibility of significant participation by the Canadian groups and potential for financial contributions from the Canadian funding agencies, for example providing the detector enclosure. Should these possibilities materialize, the Mine Centre site would be very attractive.

Near Detector

Beam-related backgrounds to $\nu_\mu \rightarrow \nu_e$ charged current events will come from beam ν_es, neutral current events, and ν_μ charged current events in which the muon is not identified. In a simulation to be discussed below, the percentages of backgrounds from these three sources were 59%, 36%, and 5%, respectively. The most straightforward method of measuring these backgrounds is to place a near detector at the same angle to

the beam as the far detector and use the same technology. The first two of these backgrounds, beam ν_es and neutral currents, will scale approximately as $1/L^2$ between the two detectors. However, the third background, ν_μ charged current events in which the muon is not identified, will not scale the same way due to oscillations. The signal from it in the near detector will be approximately three times higher than in the far detector. To make this correction, it will be necessary to estimate the relative number of neutral and charged current event backgrounds in the near detector. This can be done by measuring the ν_μ charged current events in which a muon is identified and extrapolating to the number in which the muon is not identified, using Monte Carlo simulations, or the results of other measurements. Since, in any case, the fraction of background from the ν_μ charged current events is small, this should be able to be done to sufficient accuracy.

There is a suitable location for the near detector in the NuMI tunnel upstream of the MINOS near detector hall. Little work has been done so far on the design of the near detector, and this will be one of our priorities in the coming months.

Cosmic Ray Backgrounds

The cosmic ray background will be strongly suppressed by the very low duty cycle of the accelerator beam (10 μs spill every 2 seconds resulting in a livetime of about 100 s/yr), directionality of the incident neutrino beam and its relatively high energy (1.5-2 GeV). Our preliminary estimates, described below, indicate that this background should not be a problem. Furthermore, this background can be measured with very high precision during the off-beam time. It is also our intention to test our estimates in a subsidiary experiment on the surface during the next year using a small version of a proposed detector.

The atmosphere behaves as a 10-interaction length, 25-radiation length calorimeter for the incident primary cosmic rays. The results of interactions in the atmosphere are extensive air showers, some of whose components persist to the surface: penetrating muons with 4 GeV average energy, showering electrons and photons with average energies in the range of tens of MeV, and some hadrons, primarily neutrons, with average energies in the hundreds of MeV range.

The muon flux at the surface of the earth yields an average of 13 muon trajectories inside the detector per 10 μs spill-gate and a total of 1.3×10^8 muons per year in the far detector during the active spill. These muons (actually the ones outside the active spill) provide an essential calibration and alignment tool. Muons themselves can only simulate our signal through their interactions in the detector. In a segmented detector, it is possible for muons to pass through absorber layers without being detected in the active scintillator. These muons can generate a possible background if they interact hadronicly and produce a charged track along the direction of the neutrino beam from Fermilab. We estimate that 1000 interactions per year will produce a pion of energy 2 GeV or more within the detector's fiducial volume. The overall energy flow in these interactions is orthogonal to the beam direction. Thus the probability that a track should appear electron-like, with the appropriate energy and interaction topology appears quite low.

However, we propose to place an active shield of scintillator modules around the outside of the detector.   This would be a relatively easy and inexpensive way to efficiently indicate the presence of in-time muons responsible for such events and make the background negligible. The area of shield detector required is only about 3% of the total active scintillator planes used in the detector. Assuming that the shield scintillator strips are arranged parallel to detector layers, an interaction in a specific gap would be directly correlated with a corresponding scintillator strip.

A significant flux of electrons and photons from the extensive air showers survives at ground level. The net flux is about 50% of the muon flux, but the average energy is less than 100 MeV. They will generally produce small showers that penetrate short distances (less than 1 m typically) into the top of the detector. Only about 2% have energies above 1 GeV and are capable of producing a significant shower at the top of the detector, causing multiple hits in the scintillator strips.

A small component of hadrons survives to ground level. Neutrons are the most significant; they have an interaction length of about 1.5 m in the absorber material and their interactions are therefore a potential source of background. Their trajectories are much more vertical than the muons, with average angle of 20° from the zenith, and their median energy is 100 to 200 MeV. We estimate that 1.0×10^5 neutrons with energies above 2 GeV will interact in the detector per year within the neutrino spill gate; they will be concentrated near the top of the detector. Even though neutrons at ground level are always accompanied by muons or electrons, this fact is not very useful as a veto for neutrons entering the detector because of large typical spatial separation. In the few GeV energy region, about 20% of the inelastic neutron interactions produce a single pion, which, in principle, might simulate an electron track. A pion from a neutron interaction must be emitted at an angle at least 60° to provide a possible background to a beam neutrino event. With the addition of a topology requirement that the track should be electron-like, we estimate that background from neutron interactions will be at the level of only about 1 event/year.

We plan to conduct a test with a prototype detector to check this calculation. If the backgrounds from cosmic rays turn out to be more serious than the above estimates indicate, a passive overburden could be added to the detector, at a substantial cost increase for the enclosure. The neutron flux would be reduced a factor of 100 by a dirt or rock overburden of 500 g/cm^2, about 2 to 2.5 m. Additional neutrons may be produced by the muons in the overburden, but those will be readily rejected by the presence of the parent muon nearby, either in the detector itself or in the active shield.

Proton Beam Requirements

It will become clear from the discussion of physics capabilities below that this experiment will be statistics limited. The sensitivity of the experiment will depend on the product of the detector mass and the neutrino flux. The latter is to a very good approximation proportional to the number of protons that can be delivered to the NuMI

target. An optimization of the experiment clearly involves investing in both the detector and the beam intensity. However, the latter has potentially much broader usefulness for a wide variety of future physics programs for Fermilab, and thus may be attractive beyond a simple optimization of this experiment.

The NuMI beam will begin operation in 2005 with an expected 2.0 to 2.5×10^{20} protons on target per year (pot/yr). We expect that there will be incremental improvements in the beam intensity in the next few years, as outlined by the Finley Committee. Our best estimate is that we can expect to run this experiment initially with 4.0×10^{20} pot/yr, and we will use this value in the discussion of physics potential below.

We are encouraged by the inclusion of a proton driver in the recently announced Secretary of Energy's "Facilities for the Future of Science." A 2 MW 120 GeV proton beam will greatly extend the power of this experiment. In the discussion of physics potential we will assume that such a facility will deliver 20×10^{20} pot/yr. and that the NuMI beamline facility will be appropriately upgraded, if necessary.

Simulations

We have done a number of simulations of the various detector options and siting options. All of the simulations are complete in the sense that they start with Monte Carlo simulations of raw hits in the detector, reconstruct them, and separate signal events from calculated backgrounds by the use of cuts on significant variables and then on likelihood functions of a number of variables. In these simulations, it is assumed that the size of the background is perfectly known and that the efficiency of the detector is perfectly known from the Monte Carlo simulation. In the real experiment, these quantities are determined from the near detector data, as discussed above. In the discussion of physics potential, we add a 5% error on the background determination to allow for systematic effects in this determination.

All of the simulations are optimized to a figure of merit (FOM) defined as the signal divided by the square root of the background. This optimization tends to have a flat region as a function of the ν_e efficiency, so different simulations have optimized to different points (i.e., relatively low numbers of signal events with low backgrounds as opposed to higher numbers of signal events with considerably higher backgrounds). We will summarize the results of the different simulations at the end of this section. To give and indication of how these simulations proceed, we will briefly discuss below a recent simulation, which is an explicit calculation for the baseline detector sited at our currently favored site, and which uses the latest Monte Carlo simulation of the underlying physics. However, simply for reasons of time, the discussion of physics potential which follows will be based on an earlier simulation, which optimized quite differently. We will redo these calculations for the proposal.

It should also be noted that whereas the proper FOM for observation of an effect is the one we have used, $s/b^{1/2}$, where s and b represent signal and background,

respectively, the proper FOM for extracting information from a signal is $s/(s+b)^{1/2}$, which in general will optimize differently.

Recent simulations use the NEUGEN3 event generator, which has a number of improvements over the NEUGEN2 event generator used in earlier simulations. The most important changes are
    (1) the inclusion of coherent pion production,
    (2) modifications to the resonance model to restrict unphysical event generation at high W,
    (3) improved treatment of the kinematic regime of resonance and deeply inelastic scattering (DIS) overlap,
    (4) improved treatment of DIS hadronization into specific exclusive final states, and
    (5) nuclear absorption and the inclusion of formation zone effects in the simulation of the intranuclear hadronic cascade.

One recent set of simulations directly compared the two event generators and concluded that the use of NEUGEN3 instead of NEUGEN2 reduced the FOM by 16±4% and that the reduction was consistent with being entirely due to the inclusion of coherent pion production. Another set of simulations directly measured the increased background from coherent pion production and concluded that it reduced the FOM by 7±4%. Since different simulations will optimize differently, these simulations are not inconsistent.

The baseline simulation proceeded by first identifying the most significant track-like element in an event through the use of a Hough transform. Then a rough set of cuts were placed on the character of the event and the character of the track within the event:
    (1) event length between is 2 and 7 m,
    (2) total pulse height is between 8000 and 18000 photoelectrons,
    (3) the track contains at least 70% of the hits in the event,
    (4) the average number of hits per plane is greater than 1.5, and
    (5) the cosine of the track to the beam direction is greater than 0.85.

Likelihood functions were then created for each class of events: $\nu_\mu \rightarrow \nu_e$ charged current events, beam ν_e charged current events, neutral current events, and ν_μ charged current events. The one and two-dimensional variables input into the likelihood functions were
    (1) the five variables listed above,
    (2) the maximum gap (i.e., planes with no hits) in the event,
    (3) the pulse height-weighted transverse rms of all hits to the straight line fit to the track,
    (4) the pulse height in the track,
    (5) the total pulse height vs. the pulse height-weighted transverse rms of all hits to the fit to the track,
    (6) the total pulse height vs. the pulse height-weighted transverse rms of the hits in the track to the fit to the track,
    (7) the total pulse height vs. the cosine of the track to the beam direction, and

(8) the total pulse height vs. the pulse height-weighted longitudinal rms of all hits.

Cuts are then made on each likelihood for a background to optimize the FOM. The results of this and other simulations are shown in Table 3. This simulation is listed as "A1." In general, different simulations cannot be compared with one another, because the differences are more likely to reflect the quality of the analysis algorithm than differences in the experimental conditions. However, simulations labeled by the same letter use similar algorithms and can be compared. Among the simulations using different algorithms, B2 and C2 should be comparable and their FOMs differ by 7±5%. Similarly, if we assume that solid scintillator detectors with no pulse height information are similar to RPCs with one-dimensional readout, then A4 and C3 should be comparable and their FOMs differ by 6±3%. We will present a set of more unified simulations in the proposal.

All of the simulations in Table 3 and the discussion of physics potential which follows assume that $\Delta m_{23}^2 = 0.0025$ (eV/c^2)^2. The most recent results from the SuperKamiokande experiment are consistent with this value, but have a central value of 0.0020 (eV/c^2)^2. An initial simulation of the FOM at this lower value of Δm_{23}^2 reduced the FOM by 21%. However, we have not yet systematically tried to optimize for this value of Δm_{23}^2.

Physics Potential

Assuming that sterile neutrinos either do not exist or do not mix with active neutrinos, there are currently three parameters of neutrino oscillations about which we have no information or only upper limits, $\sin^2(2\theta_{13})$, the sign of Δm_{13}^2 (i.e., whether the solar oscillation doublet has a higher or lower mass than the third state which mixes in the atmospheric oscillations), and the CP-violating phase δ. All three of these parameters significantly affect the rate of $\nu_\mu \rightarrow \nu_e$ oscillations at the atmospheric oscillation length. Thus, a single measurement, for example, an off-axis neutrino run at the first oscillation maximum, will be consistent with more than one set of values for these parameters. An additional measurement, for example an antineutrino run, may or may not be able to resolve all three parameters (in principle). This is illustrated in Fig. 7, which shows all of the values of the parameters consistent with a 2% $\nu_\mu \rightarrow \nu_e$ oscillation probability 10 km off-axis at an 820 km baseline. The values of $\sin^2(2\theta_{13})$, are shown on the vertical axis; the solid line represents the normal mass hierarchy (solar doublet low) and the dashed line represents the inverted hierarchy; the values of δ vary around the ellipses as indicated. The horizontal axis shows what the result of an antineutrino run would be.[1]

---

[1] Figure 7 does not include any allowance for either measurement uncertainties or uncertainties in the atmospheric oscillation parameters Δm_{23}^2 and $\sin^2(2\theta_{23})$, and to a much lesser extent, the solar oscillation parameters Δm_{12}^2 and $\sin^2(2\theta_{12})$. The following discussion of sensitivities will include the measurement uncertainties, but not the parameter uncertainties. In this regard it should be mentioned that there is a particularly nasty ambiguity associated with $\sin^2(2\theta_{23})$ if it is not equal to unity. This is because $\nu_\mu \rightarrow \nu_e$ oscillations at the atmospheric mass scale are proportional to

Label	Detector	MC	L (km)	Offset (km)	signal	Backgrounds ν_e, NC, ν_μ, total	FOM
A1	LS.	3	820	12	92.4	7.9, 4.8, 0.6, 13.3	25.3±0.4
A2	LS.	3	735	10	121.9	11.4, 7.1, 1.7, 20.2	27.1±0.5
A3	SS	2	735	10	178.3	17.5, 12.5, 3.1, 33.1	31.0±0.5
A4	SS*	2	735	10	195.6	21.9, 18.4, 4.1, 44.4	29.4±0.5
B1	RPC2	2	820	10	237.1	23.7, 17.2, 6.4, 47.3	34.5±?
B1*	RPC2	2	820	10	99.6	12.4, 8.7, 0.7, 21.3	21.3±?
B2	RPC2	2	735	10	225.8	25.3, 15.9, 6.0, 47.2	32.9±1.5
C1	RPC2	3	735	10	214.5	24.6, 21.9,3.1, 49.6	30.4±0.9
C2	RPC2	2	735	10	238.8	26.4, 16.3, 3.3, 46.0	35.2±0.7
C3	RPC1	2	735	10	211.8	23.6, 17.9, 4.9, 46.4	31.1±0.6

Table 3. Results of some simulations for $\Delta m_{23}^2 = 0.0025$ (eV/c^2)^2. In every case $\sin^2(2\theta_{13}) = 0.10$; however, no CP effects or matter effects are included. For the normal hierarchy, matter effects will increase the signal in simulation A1 by an average of 21%, B1 by an average of 17%, and the other simulations by an average of 15%. Simulation B1* is for antineutrinos; all of the other simulations are for neutrinos. The key to the detectors is LS = liquid scintillator, SS = solid scintillator, RPC1, RPC2 = RPCs with 1- (2-)dimensional readout at each layer. SS* represents a solid scintillator calculation in which the pulse height information was ignored in an attempt to approximate the RPC1calculation. It is the basis for the earlier statement that the availability of pulse height information increases the FOM by 5.4±2.4%. The MC column refers to the NEUGEN version used, as discussed in the text. The errors on the FOM reflect only the statistical errors in the simulations. No error estimate is available for simulations B1 and B1* due to a bug in the simulations that resulted in some duplicate events.

As an example, a sufficiently accurate measurement of a 4% antineutrino oscillation probability would resolve all three parameters with a two-fold ambiguity in δ. However, a measurement of a 2% antineutrino oscillation probability would not be able to resolve the mass hierarchy, regardless of its precision; a third measurement would be required.

The primary goals of the off-axis program will change with time. The first goal will be to measure $\nu_\mu \rightarrow \nu_e$ oscillations with a sensitivity approximately an order of magnitude greater than that of the MINOS experiment.[2] Figure 8 shows the calculated three standard deviation discovery limits for $\nu_\mu \rightarrow \nu_e$ oscillations in terms of the three unknown

---

$\sin^2(\theta_{23})$. If $\sin^2(2\theta_{23}) = 0.95$, then $\sin^2(\theta_{23}) = 0.39$ or 0.61, depending on whether θ_{23} is less than or greater than π/4.

[2] With a total of 25×10^{20} pot, MINOS expects to achieve an average three-σ sensitivity to $\sin^2(2\theta_{13})$ of 0.07. The 90% confidence level upper limit from the CHOOZ experiment at $\Delta m_{23}^2 = 0.0025$ is 0.14.
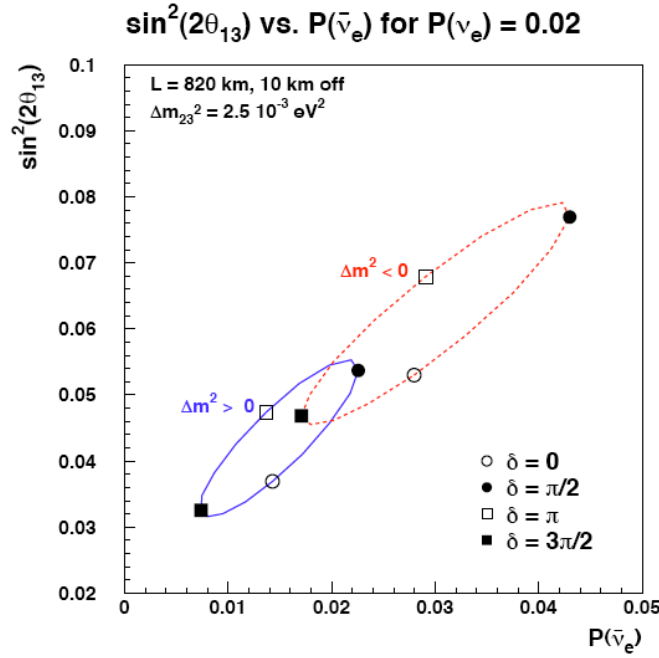
Figure 7. Plot of the possible results of a measurement of a 2% oscillation probability. See text for explanation.

parameters, assuming $\Delta m_{23}^2 = 0.0025$ $(eV/c^2)^2$. The vertical axis represents the fraction of possible δ values for which a 3-σ discovery could be made. In other words, zero represents the limit for the most favorable value of δ for a given $\sin^2(2\theta_{13})$, one represents the least favorable value of δ, and 0.5 represents a typical value. The lines represent the two possible values of the sign of Δm_{13}^2 and different assumptions on the number of protons on target (pot) that the experiment might see in a five year run. (If the figure is being viewed in gray scale, the line to the right for each number of protons represents the inverted mass hierarchy.) 20×10^{20} pot represents our estimate of what Fermilab might be able to deliver in a five-year run with incremental Booster and Main Injector improvements, while 100×10^{20} pot represents the expectation with the Booster replaced by a new Proton Driver. The 3 standard deviation sensitivity of the JPARC Phase I proposal is also shown. It is calculated for a somewhat higher atmospheric mass splitting, $\Delta m_{23}^2 = 0.003$ $(eV/c^2)^2$. This and the other calculations in this section are calculated with simulations B1 and B1* from Table 3. They are somewhat optimistic due to the use of NEUGEN2 rather than NEUGEN3.

Once a signal for $\nu_\mu \rightarrow \nu_e$ oscillations is established, the primary goal of this experiment will be to resolve the mass hierarchy. As discussed above, this can be done in some cases with an antineutrino run. Figure 9 shows the regions in which a two standard deviation (i.e., 95% confidence level) resolution of the mass hierarchy is possible with a three-year neutrino run followed by a three-year antineutrino run. The explanations given for Fig. 8 apply here as well.
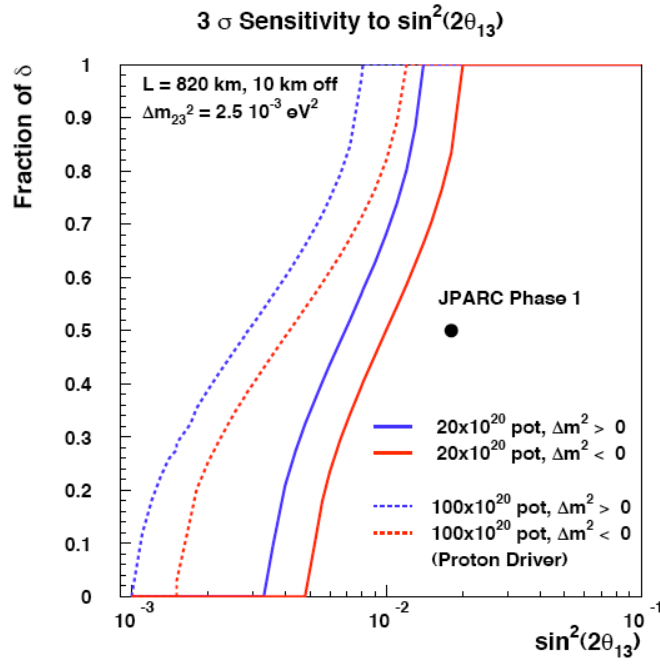
$3\,\sigma$ Sensitivity to $\sin^2(2\theta_{13})$

L = 820 km, 10 km off
$\Delta m_{23}^2 = 2.5\ 10^{-3}\ eV^2$

JPARC Phase 1

— 20×10^{20} pot, $\Delta m^2 > 0$
— 20×10^{20} pot, $\Delta m^2 < 0$

---- 100×10^{20} pot, $\Delta m^2 > 0$
---- 100×10^{20} pot, $\Delta m^2 < 0$
(Proton Driver)

Figure 8. Three standard deviation discovery limits for the observation of $\nu_\mu \rightarrow \nu_e$ oscillations. See text for more details.

$2\,\sigma$ Resolution of the Mass Hierarchy

L = 820 km, 10 km off
$\Delta m_{23}^2 = 2.5\ 10^{-3}\ eV^2$

Each ν and $\bar{\nu}$
— 12×10^{20} pot, $\Delta m^2 > 0$
— 12×10^{20} pot, $\Delta m^2 < 0$

---- 60×10^{20} pot, $\Delta m^2 > 0$
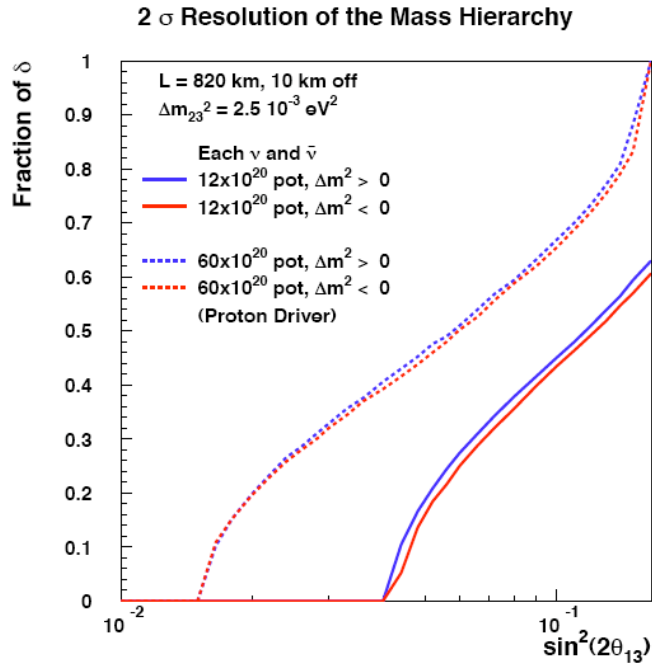---- 60×10^{20} pot, $\Delta m^2 < 0$
(Proton Driver)

Figure 9. Two standard deviation limits for the resolution of the mass hierarchy with a three-year neutrino and a three-year antineutrino run. See text for more details.

If nature chooses the parameters such that they cannot be resolved by a single neutrino and a single antineutrino run, then a third measurement will be necessary. One possibility is a neutrino oscillation measurement at the second oscillation maximum. For the NuMI beam line, this would mean moving the detector or building a new detector about 30 km off the center of the beam line. For fixed baseline, the energy associated with the second maximum is one-third of the energy of the first maximum. The second maximum gives excellent resolving power, since the matter effects decrease by a factor of three (they are proportional to energy), and the CP-violating effects increase by a factor of three (the CP violation comes from an interference term between the atmospheric and solar oscillations; the lower energy increases the solar oscillation part of the interference term). Unfortunately, the event rate is proportional to the third power of the energy (two powers from the flux and one from the cross section), so nominally the event rate will be about 27 times smaller. For this reason, the experiment is only possible with the proton intensity increase from a proton driver. Figure 10 shows the regions in which a two standard deviation resolution of the mass hierarchy is possible with a three-year neutrino and a three-year antineutrino run into two 50 kT detectors on the NuMI beamline.
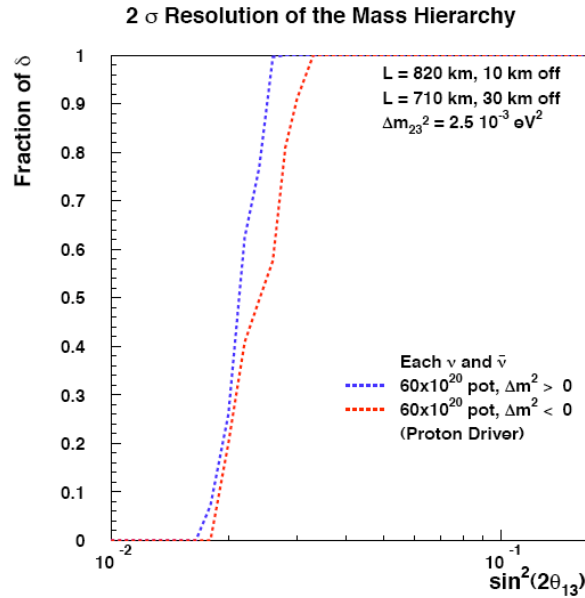

Figure 10. Two standard deviation limits for the resolution of the mass hierarchy with a three-year neutrino and a three-year antineutrino run and two far detectors. See text for more details.

Figure 11 shows the one, two, and three standard deviation contours in $\sin^2(2\theta_{13})$ and δ that would result from a measurement under the conditions of Fig. 10 for the physics parameters $\sin^2(2\theta_{13}) = 0.054$, $\delta = \pi/2$, and normal mass hierarchy.
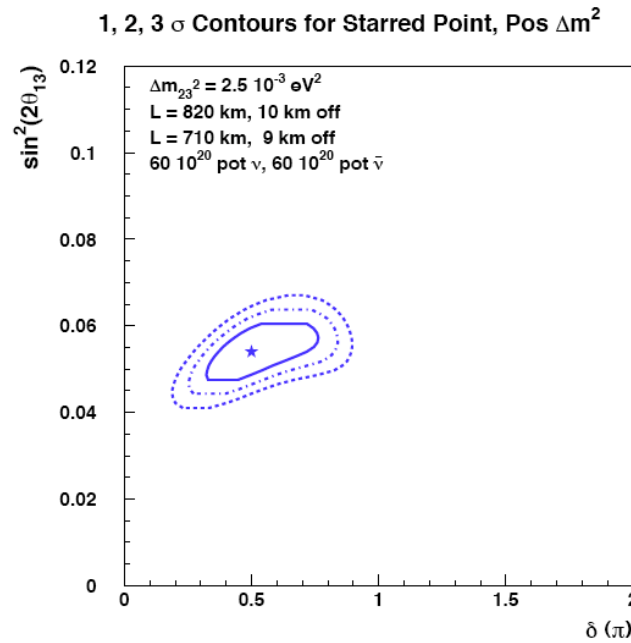
Figure 11. One, two, and three standard deviation contours for the starred point of physics parameters under the same conditions as in Fig. 10.

An alternative to a second detector on the NuMI beamline would be to combine NuMI off-axis measurements taken with a proton driver with results from JPARC phase 2. The difference in baselines between these two experiments can be exploited in high statistics experiments to provide a similar of resolution of the mass hierarchy.

Requests

As we have indicated at several points in this progress report, we need to do some crucial R&D to verify our choice of a baseline technology, to get better (and thus hopefully lower) cost estimates, and to continue engineering and design studies. We thus request that the off-axis experiment be recognized as a Fermilab R&D project at this time.

The major activities on the liquid scintillator design will include

(1) Demonstration of the system integration issues by constructing a prototype of a full plane of the detector with at least one fully instrumented prototype module capable of detecting cosmic ray events.

(2) Demonstration of the reproducibility and stability of the light output of the proposed scintillator modules, including additional aging and reactivity tests of components.

(3) Demonstration of an adequate understanding of the APD readout and electronics issues, with particular attention to the understanding of system noise issues and the integration of the necessary cooling.

(4) Verification of the production cost model through engineering work on the large scale production. Included here are design of machines to assemble the liquid scintillator modules as well as large scale structural tests and lifetime testing of absorber materials under varying conditions of humidity and temperature.

The major activities on the RPC design include:

(1) Continued development of low cost production techniques and demonstration of their performance. Included are tests of different resistive coatings, glues, and gas mixtures. A prototype of a two-gap chamber built from three glass plates will be constructed and tested. It could serve as a lower cost alternative to independent double gap chambers.

(2) Continued development of inexpensive electronics.

(3) Construction of a full-scale module, which will be subjected to mechanical test to verify its integrity and ability to be stacked.

(4) Construction of a cosmic ray test stand from a stack of 24 spare BELLE chambers to measure the level of possible confusion between cosmic ray events and ν_e charged current events. The purpose of this test is to determine whether an overburden is required for the experiment. Although we can do it most easily in the near future with RPCs, it should be a technology-independent test. We can repeat it later with scintillator modules, if necessary.

We have submitted a proposal to the NSF for support of R&D by the university groups. The requested amounts were approximately 600, 1300, and 1800 k$ for the three years of the proposal. These requests are inadequate, particularly in the first year, for all of the needed R&D, and, in particular, they do not include any funds for Fermilab and only nominal funds for Argonne. We request 489 k$ for engineering and technician effort and 170 k$ for M&S for FY 2004 for work to be done at Fermilab.. These funds are requested for development of ASICs, FESS studies of buildings, mechanical engineering support for detector construction evaluation, technician support and electronics for continued RPC prototyping, tests, the cosmic ray test stand, and evaluation of the cost of a test beam area off the Debuncher. A detailed accounting can be made available. We also request an additional 300 k$ for FY 2004, administered through Fermilab, to support efforts at Argonne and the university groups not covered by the NSF proposal. This is largely for mechanical and electronics engineering effort at Argonne in support of the R&D program.

Site consultants advise us to begin the permitting process on the Ash River site as soon as possible since it can be a lengthy process. All possible locations would be permitted while deferring the final site selection. We request 100 k$ for this process. A detailed breakdown of costs can be made available.

Appendix A: Solid Scintillator Detector

The solid scintillator detector design is essentially the same as the liquid scintillator design with the substitution of plastic scintillator modules in place of the liquid scintillator modules. The plastic strips would be conventional polystyrene-based scintillator doped with PPO and POPOP fluors co-extruded with a 0.5 mm thick outer layer of titanium dioxide loaded polystyrene, which provides a highly efficient reflector for the blue scintillation light. The plastic scintillator modules would closely resemble the MINOS modules with the exception that there would be two grooves in each scintillator to accommodate the U-shaped readout fiber.

The transverse and longitudinal dimensions of each plastic scintillator strip would be the same as that for the liquid scintillator cells, but the thickness of the plastic strips would be 1 cm instead of the 2.86 cm thickness of the liquid scintillator cells. The light output of the plastic scintillator will be approximately the same as the liquid scintillator due to the increased light output of the plastic scintillator and the better light collecting efficiency of the WLS fiber.

However, the active elements of the thinner solid modules have less mass than the thicker liquid modules (4 kT versus 8.3 kT) and, for geometrical reasons, there is less absorber mass per layer. As a result, 24% more planes (930 versus 750) are required to make up a 50 kT detector. Thus, the solid scintillator option is considerably more expensive than the liquid scintillator option for three reasons:
    (1) the scintillating material is more expensive,
    (2) more labor is required to assemble the solid modules, and
    (3) there are 24% more elements (modules, channels, etc.)

Note, however, that the absorber thickness may not be optimized, and may be changed in the proposal.

Appendix B: Resistive Plate Chamber Detector

Detector Geometry

The proposed RPC detector consists of 1,200 modules, each 8.534!m long, 2.438!m high and 2.6!m deep. Modules are stacked in an array consisting of 75 planes along the beam direction, each plane being 2 modules wide and 8 high, as shown in Fig. B.1. This design provides a high degree of hermeticity; the gap at the center of the detector between two side-by-side modules is kept to 5!mm. The distance between the modules along the beam axis is chosen to simplify the stacking and unstacking procedure and is of the order of 5!cm. The overall dimensions of the detector are 17.1!x!19.5!x!233.2!m^3.
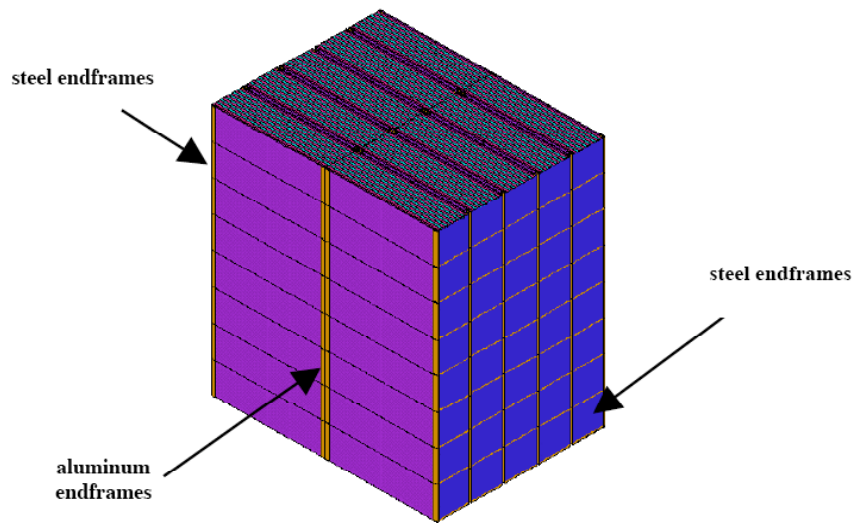

Fig. B.1. Five planes of the stacked modules.

Walls of modules are supported from the floor and are not connected to each other. Modules within each wall are interlocked with the help of corner blocks similar to those used in standard shipping containers. Readout electronics and gas distribution and recirculation lines are mounted on both sides of the detector and are readily accessible during the operation of the experiment.

Experience with large systems of glass RPCs indicates that there is no need to replace or repair them. To minimize further a potential need for replacement, this design provides redundancy by locating two independent planes of chambers at each active detector plane. It is worth noting, nonetheless, that each vertical column of modules can be unstacked without affecting its neighbors.

Module Geometry

Each module consists of 13 vertical planes of absorber interleaved with double planes of RPCs. Two end plates, Fig. B.2, provide the mechanical rigidity of the module. The weight of the module is supported by two bottom angles and subsequently transferred to four corner posts. These posts ultimately transfer the load to the floor in a manner analogous to the posts in a standard shipping container.

1/8 in. skin with 1/8 in ribs. Endframe toward center of detector array is aluminum; endframe on detector perimeter is steel.

Structural angle "shelf" for RPC and absorber support. Steel endwall uses L6x6x3/8; aluminum endwall uses L6x6x1/2.

structural side-wall absorber

12 in.

Composite particle board corner post formed by sandwiching 3 in absorber between two 1/2 inch thick aluminum plates on one end, and two 3/8 inch thick steel plates on the other.

8 rows of 5/8 in countersunk bolts, 3 bolts/row. Metal-particle board surfaces are also glued.
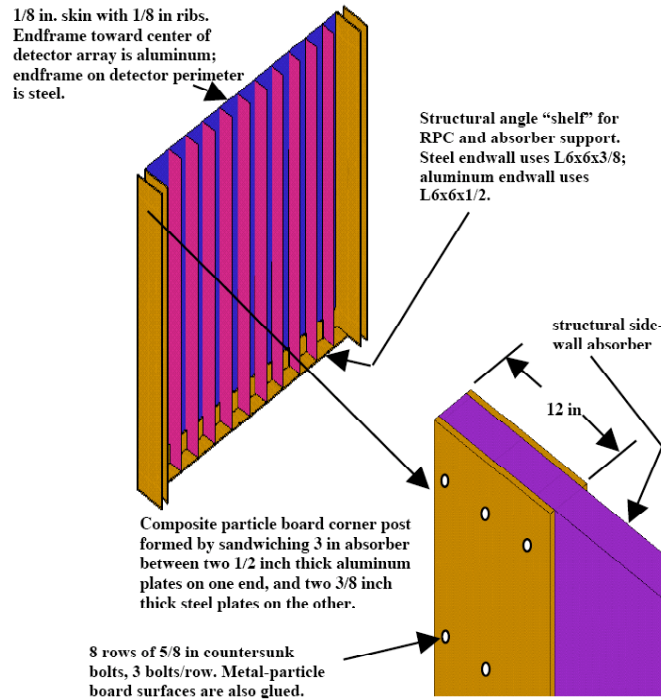
Fig. B.2: End plate and the corner post.

Absorber Planes

There are 13 absorber planes in a module. The central eleven are 10.2 cm thick and are assembled out of 4 boards 8.534 m long, 2.438 m wide and 2.54 cm thick, held together by glue and screws. The first and last absorber planes are constructed in a similar manner but are half as thick. Thus, when taken together with the first and last planes of preceding and succeeding modules, they result in a uniform sampling thickness across module boundaries. The absorber planes have 1.27 cm deep and 15.24 cm long notches at the bottom corners to accommodate the weight-supporting angles on which they rest. In addition, each of the 11 central planes is attached to a vertical reinforcing rib mounted on each of the two end plates. The support for the other two planes is provided by the corner posts, which are an integral part of them.

Detector Units

A detector unit consists of two planes of RPCs sandwiched between two particleboards, the readout boards, one carrying the horizontal readout strips and the other the vertical ones. (The option to have only one readout plane per layer, alternating between horizontal and vertical has been costed separately.) The boards also serve as protection for the glass chambers. A detector unit is 8.534!m long and 2.438!m high. It also has 1.27!cm deep and 15.24!cm long notches at the bottom corners to accommodate the weight-supporting angles on which they rest. Therefore, the chambers only cover an area of 8.509 x 2.425!m^2, resulting in a dead space due to the support structure of the order of 0.4%.

RPC Chambers

Glass RPC chambers utilize inexpensive commercial float glass of high resistivity, 10^{12} Ω cm, instead of the traditional Bakelite used in other RPCs. The RPC, shown in Fig.!B.3, is composed of two parallel glass electrodes, 3!mm thick, kept 2!mm apart by appropriate spacers. The gap between electrodes is filled with a suitable non-flammable gas mixture. The resistive coating on the outer surfaces of the glass connected to the high voltage power supply creates a strong electric field of about 4.5!kV/mm across the gap. An ionizing particle initiates a local discharge, which induces a signal on external pickup electrodes strips. The high resistivity of the glass and the quenching properties of the gas limit the discharge to a small area.

The pickup electrodes consist of a plane of metallic strips glued to an insulating layer on the other side of which is glued another metallic plane held at ground. This transforms the pickup strips into transmission lines, thus allowing the signals to be transported over long strip lengths. The induced pulses are typically 100-300!mV/50Ω with few ns time resolution. Large signals of 100-200!pC allow for the possibility of a variety of cost saving options in the readout electronics.

This type of detector does not have the rate capacity necessary for hadron colliders, but is more than adequate for low rate applications such as this neutrino experiment. This has been demonstrated by the BELLE experiment at KEK, which has successfully used them for muon and K_L detection.

Chambers are constructed in a manner very similar to the BELLE chambers. The chambers are 2.844 x!2.425!m^2 large and are constructed from 3!mm thick float glass. A uniform distance between the glass plates, which defines the electric field in the chamber, is ensured by 2!mm thick Noryl spacers placed 15!cm apart and glued to both glass plates. These spacers, glued in a maze-like pattern, serve several purposes:
   (1) They ensure a uniform gas flow over the entire area of the chamber.
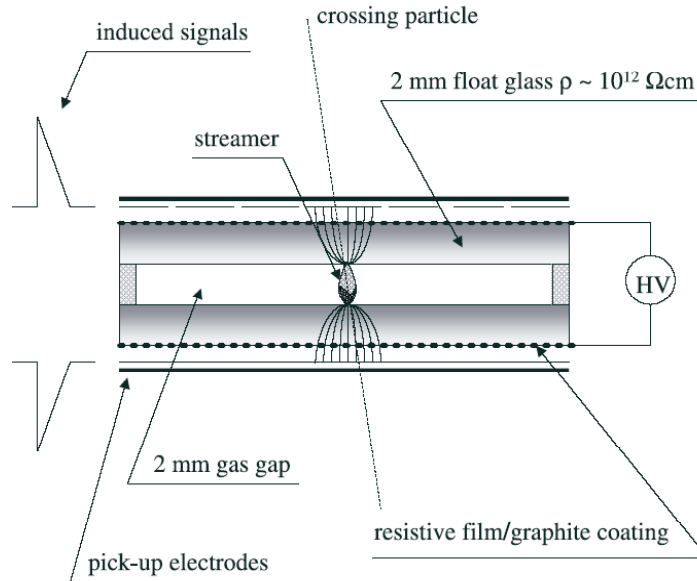   (2) They define a uniform distance between the glass plates.

Fig. B.3. Glass RPC detector principle

(3) And they protect the chamber from breaking in the event of a sudden change in atmospheric pressure. With 3!mm glass and 15!cm between spacers, chambers can withstand a difference between the internal and atmospheric pressures of up to 0.04!atmospheres (20 cm of water).

The outer perimeter of the glass plates is sealed with a T-shaped extruded Noryl border to provide a gas-tight volume. Triangular, injection molded, plastic pieces glued in the camber corners contain the gas inlet and outlet.

The outer surfaces of the glass are painted with a resistive paint. High voltage leads are soldered to a copper pad glued to these resistive layers. An insulating plastic sheet covers the entire surface of the chamber.

Readout Boards

Two particleboards, 8.534!m long and 2.438!m high, form the cover of the detector unit, with glass RPCs sandwiched between them. Both surfaces of both particleboards are laminated with thin copper foil glued to them. Copper foil on surfaces facing the chambers (inner ones) are cut into strips, the other surface is a ground plane thus creating a transmission line.

Horizontal strips are 3.7!cm wide with 3.8!cm pitch, whereas vertical strips are 4.34!cm wide with 4.44!cm pitch. One detector unit has, therefore, 192 vertical readout strips and 64 horizontal ones.

Detector Unit Assembly

Three glass chambers are positioned on the readout board to cover the entire active area. Daisy-chained gas lines provide a common gas flow for the entire plane. High voltage power supplies are separate for every chamber. Gas lines and high voltage lines are fed from the outer edge of the unit. A second plane of gas chambers is positioned on top of the first one. The spacers of chambers in the two layers are displaced with respect to each other to maximize the detection efficiency. A second particleboard with readout strips is positioned and secured with the help of bolts piercing the assembly in the region of the triangular corner pieces. U-shaped clips at the bottom of the unit support the weight of the chambers.

Signal Collection

The RPC signals are analyzed by discriminators packaged in a 64-channel chip, to be described below. Discriminator chips are mounted on interface boards that are in turn mounted directly on the readout boards. Signals from the readout board strips are collected and transported to connectors on the interface board. We propose to use flexible (flex) circuit boards and flat conductor cables as the collection and transportation path. We will try to maintain the transmission line impedance of the readout strips (about 100 Ω) in the collection and transportation scheme. Additional R&D is necessary to determine extent to which this will be necessary or possible.

A single-sided flex circuit board has been designed with 32 pads on the same pitch as the readout strips, as shown in Fig.!B.4 (not to scale). The pads are glued face down on the end of the readout strips with an adhesive that makes connections through the glue, but does not conduct between pads. The circuit has a 32-channel fan-in to a neck 6.5 cm wide. Mating to the conductors at the neck of the flex circuit, and permanently attached by the manufacturer, is a 32-channel flat conductor cable with 1 mm wide conductors on a 2 mm pitch.

The flex circuits bend over the edge of the readout board, lie flat and are taped against its backside. Separating the flex circuit from the back conductor is a dielectric sheet. The thickness of the dielectric is chosen to match the fan-in and cable impedance to the impedance of the strips. The cables must make 90° folds to reach the outer edge of the boards. In each fold it may be necessary to insert a conductor and (or) the proper thickness of dielectric to prevent an impedance mismatch. At the outer edge of the readout boards the flexible flat conductor cables will insert and lock into mating connectors on the discriminator interface cards. The flat conductor cable will extend beyond the end of the readout boards but will fold back into a 2.5 cm wide slot, created by attaching a another particleboard "spacer" on the back side of each readout board, as shown in Fig. B.5.
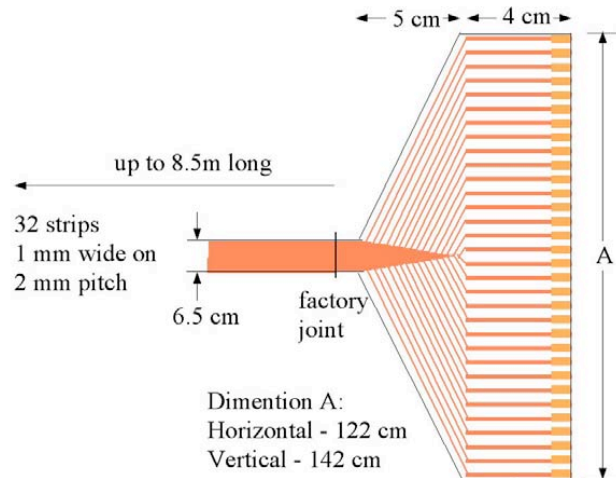
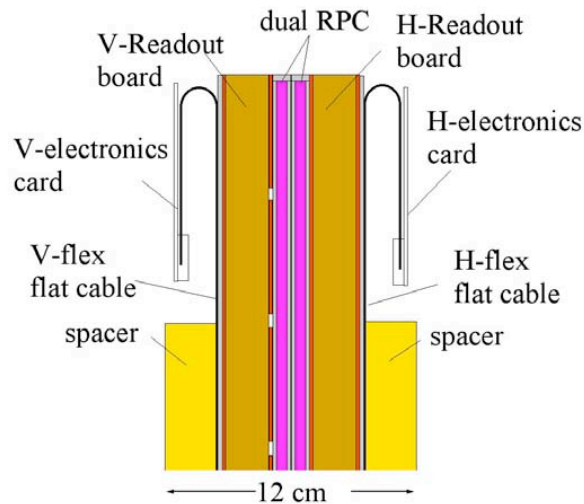Figure B.4. Signal collection flex-circuit and flat conductor cable.

Figure B.5. Routing of flat conductor cables to allow connection to discriminator interface cards.

This arrangement is designed so that electronics can be mounted and tested on the RPC detector package. Without modification, the package can then be inserted into an absorber module.

Readout Electronics

When operated in streamer mode, RPC detectors produce a large pulse in response to the ionization within the gas. The signals are large so that a significant voltage (100 mV or more) can be developed across a 50 or 100 Ω resistor. Because the measurement of

events requires only the observance of hits in the detector, it is sufficient to use a simple discriminator as the front-end electronics, without the need for additional amplification or signal processing. To facilitate event reconstruction, the output of each discriminator would latch a timestamp.

Because the data rate is low, it is envisaged that no trigger hardware is needed. Instead, the formation of a trigger and the analysis of events are done using a series of processors. This is similar to the data acquisition system of MINOS. The initial sorting of hits by timestamps is done using a VME-based processor in the front-end crate. The processor would form "time frames" using the time-sorted data. The time frames are then sent to a trigger processor, which receives time frames from the entire detector. The trigger processor runs algorithms that look for tracks and discard noise hits. Those events that pass are either written to disk, or passed to another processor for further analysis.

The functionality of the basic system described above would be configured into several basic components: the front end 64-channel ASIC, which processes the detector signals and forms timestamps; the data concentrator, which coalesces data streams from the front end ASICs to reduce the number of readout boards; the data collector, which is a VME board that receives the data streams from the front end, and makes data available for readout by the front end processor; and the trigger farm, which performs the event reconstruction, triggering, and event selection.

Table B.1 summarizes the parameters of the RPC detector.

Performance of RPCs

The performance of RPCs has been studied in the laboratory using a cosmic ray telescope and a set of small size prototype chambers. Each prototype is 25!x!25 cm^2 and is built out of two 2-mm thick glass plates. The trigger was provided by a three-fold coincidence of scintillation counters the size and position of which ensured that triggering particles traversed the chambers under study. Three chambers were stacked between the counters.

The efficiency of these chambers as a function of high voltage is shown in Fig.!B.6. It reaches 92% at 8.3!kV and remains flat for several hundred volts beyond this voltage. The dead space introduced by the spacer can account for about 1 to 2% out of the 8% inefficiency.

As was done in the BELLE detector, the 8% inefficiency of RPCs will be substantially reduced by sandwiching two RPCs between a single pair of readout planes resulting in each readout plane being sensitive to the sum of the pulse heights generated

Detector mass	50 kT
Active detector mass	4.5 kT
Detector height	19.5 m
Detector width	17.1 m
Detector length	233 m
Absorber	Particleboard or OSB
Absorber density	0.70 g/cc
Active detector	Glass RPC
Active detector module	Single gap chamber
Chamber height	2.425 m
Chamber width	2.844 m
Strip width	3.80 cm horizontal, 4.44 cm vertical
Strips per module layer	256
Chambers per module layer	6 = 3 double-gap chambers
Module layers per module	12
Number of modules per plane	16
Number of planes of modules	75
Total number of modules	1200
Total number of module layers	900
Total number of chambers	86,400 = 43,200 double-gap chambers
Total number of strips	3,686,400

Table B.1. Parameters of the RPC detector with two-dimensional readout at each layer. For one-dimensional readout at each layer, divide the number of strips per module layer and the total number of strips by two. Other parameters are the same.

by the streamers in both RPCs. Furthermore the position of the spacers in the two RPCs will be staggered so as not to overlap.
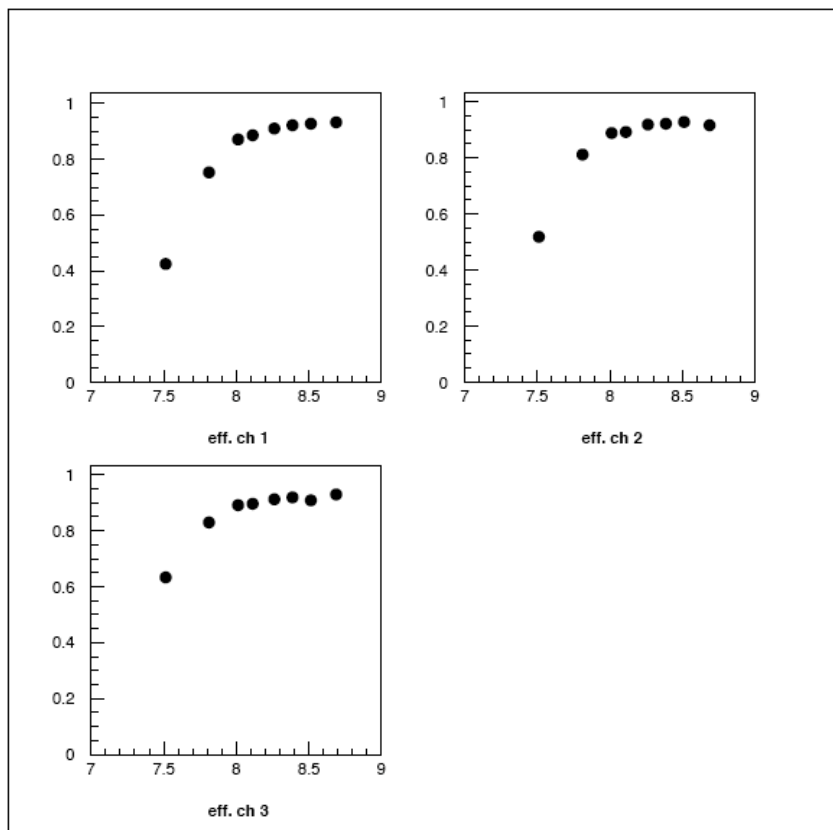
Figure B.6.   Efficiency as a function of high voltage for three chambers.